A three-dimensional cell culture platform for long time-scale observations of bio-nano interactions

Francesco Muraca[a], Amirah Alahmari[a], Valeria A. Giannone[a,b], Laurent Adumeau[a], Yan Yan[a,b], Mura M. McCafferty[a*], Kenneth A. Dawson[a*]

a: Centre for BioNano Interactions, University College Dublin, Belfield, Dublin 4; b: School of Biomolecular and Biomedical Science, University College Dublin, Belfield, Dublin 4.

* kenneth.a.dawson@cbni.ucd.ie, mura.mccafferty@cbni.ucd.ie: Correspondence should be addressed to these authors.

SUMMARY

We know surprisingly little about the long-term outcomes for nanomaterials interacting with organisms. To date, most of what we know is derived from *in vivo* studies that limit the range of materials studied, and the scope of advanced molecular biology tools applied. Long-term *in vitro* nanoparticle studies are hampered by a lack of suitable models, as standard cell culture techniques present several drawbacks, while technical limitations render current 3D cellular spheroid models less suited. Now, by controlling the kinetic processes of cell assembly and division in a non-Newtonian culture medium, we engineer reproducible cell clusters of controlled size and phenotype, leading to a convenient and flexible long-term 3D culture that allows nanoparticle studies over many weeks in an *in vitro* setting. We present applications of this model for the assessment of intracellular polymeric and silica nanoparticle persistence, and found that hydrocarbon based polymeric nanoparticles undergo no apparent degradation over long time periods with no obvious biological impact, while amorphous silica nanoparticles degrade at different rates over several weeks, depending on their synthesis method.

Keywords: 3D cell culture, cell cycle, quiescence, bio-nano interactions, nanoparticle persistence, nanoparticle degradation, silica nanoparticles

Nanostructures can gain access to biological (intracellular and other) compartments where they may accumulate and slowly degrade, producing various by-products.[1–4] This differs from the more familiar scenarios of small molecules having short *in situ* cellular half-lives, or macroscopic material implants exposed to extracellular degradation, so it is unclear what can be learned about the fate of particles by analogy to those situations.

Broadly speaking, nanoparticle populations present diverse biomolecular surfaces leading to 'scattergun' interactions with various cells, tissues and organs (including the liver).[5–12] There they will be incorporated and processed within endogenous intra- and trans-cellular trafficking pathways;[13–15] however, instead of being cleared rapidly, they may be retained for extended periods of weeks, months, or longer.[16–19] This could lead to persistent signalling dysregulation or other adverse biological processes, and the slow degradation of the particle to secondary (and other downstream) metabolites.[20–24] Given this diversity of interaction modalities, in early explorations it was surprising for some that few detrimental biological effects were observed for 'passive' materials, not otherwise chemically toxic. Still, it must be emphasised that much of what we currently know comes from short-term *in vitro* cell-level studies extending over hours,[21,25–29] with limited information on the consequences of longer-term intracellular nanoparticle localisation. This is primarily due to a lack of suitable *in vitro* models to address this issue, as commonly used cell culture systems fail to capture the complex *in vivo* environment, and are unsuitable for long-term nanoparticle studies due to rapid dilution of the intracellular nanoparticle load by cell division.[30,31] Thus, with the exception of a few studies that apply cell spheroids,[32–36] the little information available on long-term particle accumulation, degradation and cellular responses is largely observational and limited in scope, being derived from specialised *in vivo* studies.[19,23,37–40]

Rather topical examples where simplified models could shed some highly desirable light on their long-term impacts include polymeric and silica nanoparticles. Polymeric nanoparticles are either manufactured, or result from degradation of bulk polymers in the environment, and silica nanoparticles are widely used in industrial processes. Currently, the systematic study of these issues (without the use of animals), is essentially blocked.

Here we describe a highly reproducible, long-term three-dimensional (3D) culture model of small cellular assemblies that possess the architecture and some *in vivo* phenotypical features that are particularly suitable for studying long-term nanoparticle exposure. They may be created using immortalized cell lines, without the deficits suffered by dividing cells. As these cell clusters assemble, they re-form inter-cellular junctions, and restore functions known to predominate in the native tissue. Moreover, the cells transition to a quiescent state, while remaining metabolically active, thereby avoiding the confounding effects of cell division. The architecture of these assemblies is well defined, and the arrangement of cells is such that most are accessible to the cluster surface, ensuring viability over many weeks and months. These cell clusters possess ideal characteristics for studying the long-term effects of nanoparticle exposure *in vitro*, and are applied here for the assessment of polymeric and silica nanoparticles over several weeks.

Results

Long-term cell cluster architecture for nanoparticle exposure: We grow controlled cell clusters by suspension of dividing cells in a non-Newtonian polymeric additive (hereafter referred to as suspension media) that acts as a low viscosity liquid at shorter length and motional time-scales, while damping motion at longer length and time scales. This allows for diffusion of nutrients and nanoparticles, while whole-cell motion is slow and multi-cell motion is essentially quenched. While attempts to improve control of cell cultures using the viscoelastic

properties of media have been discussed previously,[41] our exploration suggests this may be an important dimension in the creation of organoid-like structures in future. There are numerous approaches to achieving control over culture media viscosity at the different length scales (tens of nanometres to micron). Soft-gelling polymer complexes have the convenience that they are readily optimised by dilution, small changes of ionic strength or other simple experimental control parameters. Examples we have explored include an enzyme modified galactomannan (Guar gum) and xanthan blend additive.[42] There are many ways of achieving similar relevant viscoelastic responses, so for simplicity our results are based on a standardised and widely available formulation.

By tuning the viscoelastic properties of the suspension media, we can control the reproducible formation, and structural and functional evolution of small cell clusters. Besides the fundamental issue of cell growth and assembly kinetics (about which we still have much to learn), there are also other practical optimisations, such as the avoidance of cell dropping or attachment to the bottom of the plates by applying an agar coating before cell seeding in the suspension media (Figure 1a). A549 human lung epithelial cells have been used for the work presented here, and we also report the possibility to reproduce these characteristics with other cell lines (Supplementary Figure S1).

Cluster growth kinetic stages: The basic kinetic processes of cell cluster formation are deduced from different regimes of time-lapse microscopy captured over 5 days (Supplementary Videos 1-7), with more detailed imaging and analysis used to follow the outcome in a quantitative manner. Early on, single 'itinerant' cells within the medium can move relatively short distances and divide; therefore, during the first several days, cell-cell associations primarily arise from engagement (collision) of nearby cells, and cell division. During this 'core formation' stage some cells engage briefly before continuing to move while others attach, leading to small core

clusters of two or three cells, after which, adjustments of cluster shape take place. After twenty-four hours there is progressive crossover to the second 'cluster-maturation' kinetic stage in which the (near-stable and increasingly immobile) 'core' clusters grow, partly via collision with itinerant cells and proximate small clusters, and partly by division of cells within the cluster (Supplementary Figures S2, S3). We also observe other rarer processes; for example, a cell (or two) that lies between two neighboring clusters can form a bridge between them to promote their merger. 'Cluster stabilisation' commences around day five, wherein most of the itinerant cells are exhausted, rapid cluster growth ends, and established clusters are essentially immobile (Figure 1b).

Cluster size and shape evolution: The distribution of the major (long) axis length of the growing and maturing clusters exhibits a tail and is therefore not strictly Gaussian (Figure 1c, Supplementary Figure S4 and Supplementary Table S1). While the origin of this small proportion of larger cluster size is not yet fully understood (it could be due to some cells reaching the agar-coated surface and forming slightly larger structures), if we extract a median or mean size from the distributions over time, the most rapid cluster size increase indeed accompanies the cluster growth stage, and changes slow dramatically after the first five days (Figure 1d). At the cluster stabilisation stage, the minor axis begins to be approximately described as a bilayer of cells. The fact that clusters are restricted in size (typically less than 100 μm; Figure 1c-e and Supplementary Figure S4) and oblate in shape (Figure 1f and Supplementary Figure S5) means that most cells have access to nutrients, gas supply and waste clearance,[43] and thus remain viable throughout the culture time (Supplementary Figure S6). The clusters can be easily isolated and used for many practical purposes after the first week in culture.

Evolution of nanoparticle-relevant cellular function accompanying cluster growth: While there are many changes in cell morphology, ultra-structure, function and phenotype occurring

during cluster formation, it is not always clear to what degree they drive, or are a consequence of, multi-cell assembly. A broad proteomics screening comparing A549 clusters with the same cells grown as monolayer revealed major changes in the phenotype of the clusters. There is a shift toward a quiescent, secretory phenotype after the first week of culture (Supplementary Figures S7, S8, S9). Moreover, an increase in ROS defence coupled with increased mitochondrial activity and fatty acid metabolism suggests that a deep metabolic alteration, consisting of a shift toward a more ROS resistant phenotype, is occurring within the clusters in suspension.[44,45]

Cell-cell adhesion is fundamental for the stability of biological tissues, providing structural rigidity and other functional cues.[46] Compared to monolayer cells where the main cell interactions occur with the culture substratum, the clusters form strong cell-cell interactions immediately upon contact.[47] E-cadherin mRNA expression is upregulated in cells organised in clusters in the suspension media compared to monolayer grown cells, and the protein is more strongly presented at the cell surface and interface, consistent with cell-cell adhesion complex formation (Figure 2a-c and Supplementary Figure S10).

With the formation of clusters, an increase in cell secretory events was observed. There is a significant increase of mucin 5AC and IgG Fc binding protein mRNA expression in the cell clusters compared to monolayer, and wheat germ agglutinin (WGA) staining revealed a thickening and rearrangement of surface carbohydrate residues containing sialic acid and N-acetylglucosamine residues, consistent with increased respiratory mucus secretion[48] (Figure 2d-g, and Supplementary Figure S11). TEM micrographs of clusters confirm that there are numerous secretory granules and vesicles within the cells after the first week of culture, with secretion of different materials (Figure 2h,i and Supplementary Figure S12). Additionally, some lysosomal activities seem to be differently regulated in the clusters, with increased expression of cathepsins and other important transcription factors, which could be related to

150 extracellular matrix remodelling (Supplementary Figure S13). Taken together, these results
151 indicate that the A549 cell clusters grown in this way possess characteristics that more closely
152 represent their native *in vivo* phenotype, compared to the same cells cultured in monolayer.
153 *Nanoparticle uptake, dilution, and trafficking in dividing and quiescent cell states:*
154 Traditionally, understanding the uptake and trafficking of nanoparticles in monolayer cells is
155 complicated by the fact that upon division, cells split their intracellular contents between
156 daughter cells, thereby diluting the nanoparticle load. Therefore, the establishment of a
157 quiescent state in the cells organised as clusters is critical for the long-term assessment of
158 nanoparticle interactions. A time-resolved cell cycle analysis of the clusters determined that all
159 but the G0/G1 phases are depopulated during the first week (Figure 3a, b and Supplementary
160 Figures S14, 15). After two weeks there are no cells in the S phase, while cell viability remains
161 largely unaffected. Furthermore, $p27^{kip1}$ (a G1 cyclin complex inhibitor critical in the
162 maintenance of quiescence[49]) mRNA expression is increased (Figure 3c). Consistent with this
163 finding, Ki67 antigen (a proliferative cell marker) mRNA and protein expression is almost
164 completely downregulated in matured clusters (Figure 3d, e, f, and Supplementary Figure S16).
165 Together, these results suggest that the cells have exited the cell cycle and entered the quiescent
166 (G0) phase. When cells are recovered by disassembly of the clusters and reconstituted into
167 monolayer, they rapidly restore normal cell cycling, even after up to 3 weeks of cluster culture
168 (Supplementary Figures S17, 18). We therefore believe that the cell clusters have established
169 a quiescent state, which (given the intrinsic limitation of using rapidly dividing cells) is more
170 useful for application in long-term nanoparticle studies.
171 For the cluster model presented here, cells can be exposed to particles either prior to or after
172 formation of clusters, and the outcomes studied over many weeks (during which the cells are
173 in their quiescent state). We present results for these exposure scenarios using polystyrene
174 carboxylate-modified nanoparticles (PS-COOH NPs), conventionally considered non-

175 degradable and non-toxic. For the pre-cluster formation exposure method (Figure 4a), cells in
176 monolayer were exposed to particles for 4 hours (0.1 mg/mL), then seeded in the suspension
177 media to form clusters. Within the first days of cluster culture, the nanoparticle fluorescence
178 loss is reduced, and after several days there is little further decrease. Indeed, for some weeks
179 thereafter there is no significant change in the quantity of nanoparticles in cells in clusters nor
180 any evident cell cycling, while the dividing monolayer cells have lost their nanoparticle
181 population due to dilution (Figure 4b, c, d and Supplementary Figures 19). Confocal
182 microscopy imaging suggests that most particles remain localised within lysosomes during
183 those extended periods (Figure 4e and Supplementary Figure 20).
184 Significantly, this model allows for another exposure scenario, in which living quiescent
185 suspended cell clusters can be treated directly with nanoparticles (Figure 4f). Clusters (grown
186 for 1 week) were treated in the suspension environment with 0.02 and 0.1 mg/mL PS-COOH
187 NPs for 4 hours, and a higher uptake was observed for both particle concentrations, in
188 comparison with monolayer cells (Figure 4g, h, i and Supplementary Figures S21, 22). While
189 there is still much to be learned about nanoparticle uptake and trafficking in these clusters, one
190 key observation is that most cells in the cluster are exposed to particles, although at different
191 levels, seemingly irrespective of their location (Figure 4 j, k, l, m, and Supplementary Figures
192 S22, 23). Immediately after nanoparticle treatment, some particles can be seen on the surface
193 of the cells, especially at the mucus interface (Figure 4j, k); however, 24 hours after treatment,
194 particles are no longer observed on the surface of the clusters (Figure 4l, m). The fact that many
195 particles are present even in cells that seem to have their external surface completely covered
196 with mucus suggests that nanoparticles can reach the cell membrane and be internalised, even
197 in the presence of thick mucus layers. Also, as most cells are already in their quiescent state
198 when treated, there is little dilution of nanoparticles due to cell division, even after many weeks
199 (Supplementary Figure S24). The minimal loss of particles from the cell clusters is an expected,

200 but significant, confirmation that much of the apparent dilution of intracellularly accumulated
201 particles observed in recent years is indeed directly related to cell division.[30] These results also
202 give us a first opportunity to meaningfully investigate the long-term consequences of
203 intracellular nanoparticle accumulation.
204 *Modelling long-term nanoparticle exposure and degradation scenarios:* While it is not our
205 intention here to report on exhaustive studies of long-term nanoparticle exposure, it is clear
206 that the quiescent cluster model will allow a detailed mechanistic insight into the evolution of
207 nanoscale materials inside living organisms. Using the exposure system described above, we
208 illustrate the potential for valuable outcomes using examples of different types of silica
209 nanoparticles, a material of significant practical interest. While silica has long been considered
210 biodegradable in biological milieu, it is less well understood that this question is a matter of
211 the material structure (dictated by the synthesis processes), as well as the details of its specific
212 cellular localisation. We illustrate this using two different forms of silica: SiO_2 – an amorphous
213 silica nanoparticle, and SiO_2@SiO_2 – an amorphous silica nanoparticle coated with an
214 additional, more dense layer of silica (Supplementary Figure S25).
215 Both formulations of SiO_2 particles show extensive degradation in biological cell culture media
216 (cMEM), while there is little or no degradation in artificial lysosomal fluid (ALF) (Figure 5a).
217 Accumulation in the cell lysosomes in quiescent clusters leads to slow degradation over many
218 weeks (Figure 5b and Supplementary Figure S26, 27). The SiO_2 particle shows a higher degree
219 of degradation within the lysosomes, as changes in the surface of the particle are observed,
220 together with a decrease in particle size. Indeed, by 4 weeks in culture, some of the particles
221 are significantly degraded with a distinct architecture no longer visible. In contrast, the
222 SiO_2@SiO_2 particles remain stable in the lysosomes for longer, with minimal changes in shape
223 and size by the end of the 4 week culture period (although some etching of the surface can be
224 observed). In no case do we observe any significant biological impacts on the cultures, even

when the silica slowly degrades, and currently we believe that most (amorphous) silica will degrade over quite long periods, dependent on the specific nature of the material.

The contrast with PS-COOH NPs is striking. It appears that these cultures can be run almost indefinitely, but for our observation time, the particles appear to remain internalised, and persist unaffected. Furthermore, there is no evident biological impact on the cells during these longer times; this could suggest that polymer nanoparticle accumulation is almost indefinite, and that any biological impacts would be very subtle and require detailed biological analysis, possibly best accomplished in cultures of this type.

Conclusions

To date, most studies of long-term nanoparticle effects rely on *in vivo* animal models, which are costly and significantly different to human physiology. For materials that exhibit no chemical toxicity, long-term accumulation with few observable biological outcomes leads conventional toxicological studies to a 'dead end' in which, while there are no observable effects, the investigative tools are absent to explore novel concepts and fully determine the final outcomes.

In this work we have described a long-term 3D cell cluster culture platform produced by control of the kinetics of cellular collision, division, and phenotypic evolution. When appropriate cluster formation programs are chosen, dividing cells reach a quiescent state, coupled with the establishment of an *in vivo*-like phenotype for long periods (potentially many months). These characteristics allow for longer term observations of nanoparticle cell interactions in a more relevant environment, while preventing some of the drawbacks observed in standard monolayer culture and other *in vitro* 3D culture models. Clusters formed with this technique are reproducible, stable and viable for many weeks, and may be subjected to all the advanced tools of modern molecular and cell biology. In addition, the cells comprising the clusters are

accessible to nanoparticles, allowing for conventional uptake studies in which all the cells accumulate and retain particles in much the same way as we believe tissue does.

The need for such tools is illustrated using two different formulations of SiO_2 nanoparticles that degrade at different rates over several weeks depending on their synthesis method. Significantly, (hydrocarbon based) polymeric nanoparticles are found to undergo no apparent degradation over long time periods, nor do they have obvious biological impacts during this time. The availability of such cultures would now allow the whole range of modern biology to be deployed in the question of whether there could be as yet undiscovered subtle effects of nanomaterial accumulation over such very long periods of time. It is likely that question will attract considerable interest in the near future.

Materials and methods

Cell culture

A549 non-small lung carcinoma (ATCC® CCL-185™), HepG2 (ATCC® HB-8065™) and HEK-293T (ATCC® CRL-11268™) cell lines were purchased from ATCC, and cultured in MEM (Life Technologies) supplemented with 10% FBS (Life technologies) and 1% penicillin/streptomycin (referred to hereafter as cMEM). Cells were grown at 37˚C in a humidified atmosphere of 5% CO_2 and sub-cultured at 70-80% confluence using trypsin (0.25% in EDTA). Cells were screened monthly for mycoplasma contaminations using the MycoAlert™ Mycoplasma Detection Kit, and all cultures were free of contamination for the duration of experiments reported.

Nanoparticles

FluoSpheres™ Carboxylate-Modified yellow-green fluorescent (505/515) polystyrene nanoparticles (PS-COOH NPs; d: 100 nm) were used throughout the study (F8803; Thermo Fisher Scientific). Characterization of the particles in PBS and cMEM was performed by dynamic light scattering (DLS) measurement (Supp. Figure S28 and Table S4). Dye release from the particles under different conditions was tested by SDS-PAGE (figure S30).

Silica (SiO_2) nanoparticles were prepared as described previously.[50,51] Briefly, a fluorescein isothiocyanate - silane conjugate (FITC-APTMS) solution was prepared as follows: FITC (4 mg) was dissolved in 2 ml of anhydrous ethanol, and 20 µL of (3-Aminopropyl)-trimethoxysilane (APTMS) was added. The mixture was incubated at room temperature while shaking for 4 hours, protected from light.[52]

Preparation of the SiO_2 seeds:

A solution composed of 21.6 mL ethanol and 0.24 ml tetraethyl orthosilicate (TEOS) was added quickly to a solution composed of 21.6 ml ethanol, 1.18 ml of NH_4OH solution (28-30 % w/w) and 114 µL of water. The mixture was left to react at room temperature for 2 hours.

Growing of the SiO_2 NP to 100 nm:

A solution composed of 57.8 mL ethanol, 19.6 mL water, 1.12 ml NH_4OH (28-30 % w/w), and 7 mL of the SiO_2 seed dispersion was prepared. Then 50 µL of FITC-APTMS solution and 100 µL of TEOS were added. After 30 mins, another 50 µL of the dye conjugate solution and 100 µL of TEOS was added. Then every 30 mins thereafter, 100 µL of the dye conjugate solution and 200 µL of TEOS was added until the particles reached a diameter of approximately 100 nm. Three hours after the last addition of TEOS, the NH_4OH was removed by evaporation under reduced pressure and the dispersion was centrifuged at 14,000 g during 10 min. The SiO_2 particles were washed 3 times with water by centrifugation.

Addition of the protective SiO_2 layer:

To make the SiO_2@SiO_2 particles, the SiO_2 nanoparticles were dispersed at 20 g/L and split into 2 mL centrifuge tubes (1.5 ml/tube) then 7 µL of TEOS was added to each tube and the dispersion was heated while stirring at 90°C for 1 hour. Another 7 µL was added and the particles were incubated again at 90°C for 3 hours. The particles were then washed with water 3 times by centrifugation.

Size distribution of the SiO_2 nanoparticles was determined by DLS measurement after dispersion in water together with the zeta potential using a Zetasizer ZS series (Supp. Table S3), differential centrifugal sedimentation (DCS), considering a colloidal SiO_2 density of 2 g/cm^3 in a sucrose gradient (8-24% w/w in water), and transmission electron microscopy (TEM) (Supp. Figure S25, Supp. Table S2).

Cell seeding and nanoparticle exposure

A549 cells (2.5 x 10^6) were seeded in 75 cm^2 flasks (in cMEM) and left to adhere for 24 hours. Prior to cell exposure, PS-COOH NPs were incubated at a final concentration of 0.1 mg/mL in cMEM at 37˚C for 1 hour (to form the protein corona). Cells were exposed to this nanoparticle suspension for 4 hours at 37˚C in a humidified atmosphere of 5% CO_2, while control cells received cMEM without nanoparticles. The suspension was then removed and the cells were washed twice with cMEM and twice with PBS. After this washing step, cells were harvested by trypsinisation and used for the following experiments.

Cluster formation

Suspension media (SM) was prepared by diluting Happy Cell additive (Vale Life Sciences) from the stock solution of 4X to 1.7X with MEM supplemented with 1% penicillin/streptomycin, and FBS was added to the solution to reach a final concentration of 10%. A549 cells were harvested from monolayer culture and resuspended in SM to a concentration of 10^5 cells/ml. 24 well plates were precoated with 400 µl of 1% agarose (Merck-Sigma) in MEM as described previously,[53] and then 700 µl of ASM was added on top. 1 ml of SM containing the cells was then gently pipetted on top of this layer (this helps to avoid cell sedimentation at the bottom of the well), resulting in a final cell number of 10^5 cells/well. Cluster formation was monitored during the following days by light microscopy, and a portion of media was exchanged every other day.

Cluster harvesting

Cells in SM were harvested directly from the well and collected in falcon tubes. Inactivation solution (Vale Life Sciences) was added to the cluster suspension to a final concentration of 60 µg/ml, followed by 30 minutes incubation at 37˚C in a humidified atmosphere of 5% CO_2. After incubation, 7 ml of cMEM was added to the falcon tube to dilute the SM, and the clusters were collected by centrifugation at 1,500 RPM for 3 minutes at room temperature. Supernatant

was removed, and the cells were resuspended in an appropriate buffer dependant on subsequent processing.

Cluster disassembly and reseeding as monolayer culture

Clusters were harvested as described above every week and treated with Accutase® solution (Merck-Sigma) for 20 minutes at 37˚C in a humidified atmosphere of 5% CO_2. The solution was pipetted thoroughly every 10 minutes to help the separation of the clusters into single cells. Cells were then resuspended in fresh cMEM and seeded in 6 well plates, where they were harvested for analysis after 24 and 72 hours using trypsin.

Nanoparticle exposure to cell clusters

Prior to cell cluster exposure, the PS-COOH nanoparticles were incubated at a concentration of 1 mg/ml or 0.2 mg/ml in cMEM for 1 hour at 37˚C to form the corona. Then 10% (volume) of the SM containing clusters was removed from each well and substituted with the nanoparticle suspension and mixed well (final concentration of the NPs in the well: 100 µg/ml or 20 µg/ml). NP dispersion was checked by differential centrifugal sedimentation (DCS, Sup. Figure S29). Cell clusters treated with cMEM with no particles were used as a control. After 4 hours of incubation, cell clusters were harvested from the SM as previously described and washed twice with cMEM then twice with PBS to remove excess non-internalised particles. Clusters were then resuspended in fresh SM and cultured for extended periods (up to 2 weeks) or used immediately.

Nanoparticle uptake assessment by flow cytometry

To dissociate the cell clusters for analysis by flow cytometry, they were harvested from SM and washed once with PBS then disassembled using Accutase® solution (Merck-Sigma) as previously described. Cells were then resuspended in 150 µl of cold PBS and immediately analysed with an Accuri C6 (Becton Dickinson) with the following settings: flow rate 14 µl/min, factory laser and filter settings. To assess the cell uptake of nanoparticle, the fluorescent signal of the internalised NPs was measured (excitation/emission 488/530 nm) for ≥10000 events collected in the population gated for single cells (gating strategy is presented in Supplementary Figure S14).

Cell cycle analysis

The cell cycle of cells in monolayer or in clusters was assessed throughout the culture period using DNA and 5-ethynyl-2'-deoxyuridine (EdU) staining. Briefly, cells from monolayer culture or suspension were treated for 1 hour with EdU, clusters were disassembled and then fixed in 70% ethanol overnight at -20˚C. Cells were stained using the Alexa 488 Click-It EdU flow cytometry kit (Thermo Fisher) following manufacturer instructions. Before analysis, cells were resuspended in 1 µM Vybrant Dyecycle ruby stain (Thermo Fisher) in PBS and incubated at 37˚C for 30 minutes, then resuspended in PBS and analysed with an Accuri C6 (Becton Dickinson) with the following settings: flow rate 14 µl/min, factory laser and filter settings. For each sample, ≥10,000 events in the population gated for single cells were collected (gating strategy is presented in Supplementary Figure 14).

mRNA expression analysis

Cells were harvested from the SM or monolayer and washed once with PBS. Total RNA was extracted from cells using the Invitrap® Spin total RNA minikit (Invitek molecular) then quantified using a Nanodrop 2000 (Thermo Fisher). RNA quality was checked using a

Bioanalyser (Agilent), with all samples having an RIN number of at least 8. cDNA was then obtained by reverse transcription using the High-Capacity cDNA Reverse Transcription Kit (Applied Biosystems) following manufacturer instructions. For qPCR analysis, SYBR™ Green PCR master mix (Thermo Fisher) was used together with the primers for the following genes of interest: Ki67, p27, E-CAD, MUC5AC, IgGFc, CTSB, CTSD, CTSL1, CTSS, CTSZ, TFEB; GAPDH was used as the housekeeping gene (Supplementary Table S5). Comparative ΔCt method (ΔΔCt) was used to calculate fold change in mRNA expression of targets.

MTS assay

For monolayer cells the MTS assay (Promega) was performed following manufacturer instructions, using 1 minute incubation with 0.1% Triton X-100 (Merck-Sigma) for the positive control for cytotoxicity. For cell clusters, a modification of the protocol was necessary. Briefly, clusters were harvested from the SM as previously described, then resuspended in PBS and divided into two equal volume samples. For both untreated and NP treated samples, one of the two parts was treated with Accutase® as described and then resuspended in PBS. For the untreated sample, this part was used to count the number of cells. Based on the number obtained, a volume of the untouched clusters was taken to make a solution with $5*10^4$ cells in 1.1 ml of MTS in cMEM. Same volume was used also for the NP treated sample, assuming that same number of cells was seeded in the beginning of the experiment. Then, 110 µl of MTS solution (containing around $5*10^3$ cells in clusters for the untreated sample) were seeded in a 96 well plate in 3 technical replicates and incubated at 37˚C and 5% CO_2 for one hour. Results were then obtained by measuring absorbance at 490 nm using a plate reader (Varioskan Flash, Thermofisher).

Live/Dead staining

Live-dead staining was performed on disassembled clusters. Briefly, 3 µM DRAQ-7 dye (BioStatus) was used to stain the cells was used to stain the cells suspended in PBS and incubated on ice for 5 minutes, and the percentage of live and dead cells was recorded using an accuri C6 (Becton Dickinson) with factory laser and filter settings. > 10,000 events were recorded per sample (gating strategy is presented in Supplementary Figure S14).

Mass spectrometry analysis

Monolayer cells were washed 3 times with ice cold PBS and then harvested using a scraper. Clusters were harvested as described and washed 3 times with ice cold PBS. Following centrifugation, cell pellets were resuspended in 8 M urea lysis buffer (8 M urea, 50 mM NH_4HCO_3, and 1 mM EDTA, pH 8; reagents from Merck-Sigma) containing protease inhibitors (cOmplete mini, Roche). Short sonication was used to break the cells and to fragment the nuclear DNA, then the mixture was centrifuged at 20,000 x g for 15 minutes to pellet DNA and cell debris. The supernatant total protein was collected and quantified by BCA assay (Thermo Fisher) and 40 µg was for preparation for mass spectrometry analysis. Briefly, the total lysate was first reduced using DTT (10 mM), and alkylated by iodoacetamide (40 mM), and then digested over night at room temperature using trypsin (enzyme to substrate ratio 1:50; Thermo Fisher). Resulting peptides were purified using Pierce™ C18 high capacity tips (Thermo Fisher), and then dried and resuspended in 0.1% formic acid (Merck-Sigma). Analysis was performed on technical triplicates by electrospray liquid chromatography mass spectrometry (LC-MS/MS) using an HPLC (Thermo Fisher) interfaced with an LTQ Orbitrap

(Thermo Fisher). MaxQuant and Perseus Software (Computational Systems Biochemistry, Max Planck institute, Martinsried) were used to analyse the data.

Cluster formation timelapse imaging

Cell clusters in SM were imaged directly in their plate using a Zeiss Axiovert 200M inverted microscope with brightfield illumination and a 10x air objective. The cells were maintained at 37˚C and 5% CO_2 for 24 hour timelapse (2 hour capture increment) and 48, 72, 96 and 120 hours timelapse (3 hour capture increments), using the Zeiss software associated with the microscope. Further analysis of the images was performed using ImageJ software.

Spinning disc confocal Imaging

Cell clusters were imaged using 96-well glass bottom plates (Greinier Bio-one) on a Nikon eclipse TI spinning disc confocal microscope. Clusters were fixed and permeabilsed prior to immunostaining with 4% paraformaldehyde and 0.1 Triton-X 100 (permeabilisation was not needed for anti E-cadherin antibody). Antibodies used: Ki67 (Abcam ab92742), E-Cadherin (Abcam ab40772) and LAMP-1 (Abcam ab24170). As secondary antibody, an Alexa 546 was used in combination with every primary antibody (Thermo Fisher A11030 and Thermo Fisher A11035). Images were analysed with Imaris imaging software (Bitplane) and ImageJ. For wheat germ agglutinin (WGA) staining, the cell clusters were incubated with WGA 594 (5 µg/ml) for 15 minutes at 37˚C in a humidified atmosphere of 5% CO_2 and then washed with PBS and fixed with 4% paraformaldehyde. DAPI (2 µg/ml) was used to counterstain the nuclei of fixed cells prior to imaging. The Imaris imaging software was also used to render in 3D the images in figure 1f and S4.

High content screening

For cluster diameter assessment, cells were treated with WGA 594 and DAPI as previously described, and then imaged in 96 well glass bottom plates (Greiner Bio-one) using an Opera Phenix™ high content spinning disc microscope (Perkin Elmer). Long axis length distribution was assessed using the algorithm provided by the proprietary software (Harmony High-Content Imaging and Analysis software, Perkin Elmer). > 1,000 clusters were analysed for each timepoint.

Transmission electron microscopy

Cell clusters were washed with PBS and immediately fixed with 2.5% glutaraldehyde in 0.1 M Sorensen phosphate buffer, rinsed with Sorensen phosphate buffer, and then post-fixed for 1 hour in 1% osmium tetroxide in deionised water. Cells were dehydrated in a graded ethanol series (from 70% to 100%), followed by Acetone rinse. Samples were then immersed in an Acetone/Epon (1:1 vol/vol) mixture for 1h before being transferred to pure Epon and embedded at 37˚C for 2h. The final polymerization was carried out at 60˚C for 24h. Ultrathin sections of 80 nm, obtained with a diamond knife using an ultra-microtome Leica U6, were supported on copper grids. Sections were stained with uranyl acetate and lead citrate before being examined with an FEI TECNAI transmission electron microscope.

Statistical analysis

All data are shown as mean ± SD as described in the figure captions. $p < 0.05$ was considered significant. The experiments were performed at least 3 times independently (with exception of cell cycle analysis by flow cytometry and SiO_2 NPs degradation assessment, with 2 independent replicates, cluster size distribution with one independent replicate per operator, 2

in total (see supp. Figures S31, 32 for independently replicated data from other operators). The number of independent replicates (N) performed for each experiment is indicated in each figure caption. Statistical analyses were performed using Prism 6.01 (GraphPad software). Student t-test and one-way ANOVA, the first two-sided with Welch correction and the latter with Turkey correction for multiple comparisons, were used as described in the figure captions. Statistical differences are defined as * $p < 0.05$; ** $p < 0.01$; *** $p < 0.001$.

Conflict of interest: Authors declare no conflict of interest.

Acknowledgments: The authors acknowledge Ms J Li, Ms W Zhang, and Mr X Yang for the independent replications of some of the experiments. F.M. acknowledges the support of the Irish Research Council Postgraduate fellowship (GOIPG/2015/2530). A.A. acknowledges the Princess Nourah Bint Abdulrahman University Project Ref: IR10177, ID: 1056571209, M.M.C. acknowledges the support of the Irish Research Council Enterprise Partnership Scheme (Postdoctoral) 2019 - EPSPD/2019/232. The authors acknowledge Dr. A. Blanco and Dr. D. Scholtz from the Conway Institute of Biomolecular and Biomedical research centre flow cytometry and imaging core facilities in University College Dublin for their assistance, and Dr. A. Davies from Vale Lifesciences for the support.

Supporting Information: All supporting information is available free of charge via the Internet at http://pubs.acs.org.

Author contributions: F.M., M.M.C., and K.D. designed the experiments. F.M., A.A. and V.A.G. performed the experiments and data analysis. L.A. synthesised and characterised the two formulations of silica NP used in this study. F.M., Y.Y., M.M.C. and K.D. wrote and revised the manuscript.

Data availability: All relevant data during the study are available from the corresponding authors upon request.

1. Albanese, A., Tang, P. S. & Chan, W. C. W. The Effect of Nanoparticle Size, Shape, and Surface Chemistry on Biological Systems. *Annu. Rev. Biomed. Eng.* **14**, 1–16 (2012).

2. Blanco, E., Shen, H. & Ferrari, M. Principles of Nanoparticle Design for Overcoming Biological Barriers to Drug Delivery. *Nat. Biotechnol.* **33**, 941–951 (2015).

3. Pelaz, B. *et al.* Diverse Applications of Nanomedicine. *ACS Nano* **11**, 2313–2381 (2017).

4. Gong, N. *et al.* Carbon-Dot-Supported Atomically Dispersed Gold as a Mitochondrial Oxidative Stress Amplifier for Cancer Treatment. *Nat. Nanotechnol.* **14**, 379–387 (2019).

5. Cedervall, T. *et al.* Understanding the Nanoparticle-Protein Corona Using Methods to Quantify Exchange Rates and Affinities of Proteins for Nanoparticles. *Proc. Natl. Acad. Sci.* **104**, 2050–2055 (2007).

6. Monopoli, M. P., Åberg, C., Salvati, A. & Dawson, K. A. Biomolecular Coronas Provide the Biological Identity of Nanosized Materials. *Nat. Nanotechnol.* **7**, 779–786 (2012).

7. Tenzer, S. *et al.* Rapid Formation of Plasma Protein Corona Critically Affects Nanoparticle Pathophysiology. *Nat. Nanotechnol.* **8**, 772–781 (2013).

8. Corbo, C. *et al.* The Impact of Nanoparticle Protein Corona on Cytotoxicity, Immunotoxicity and Target Drug Delivery. *Nanomedicine* **11**, 81–100 (2016).

9. Saha, K. *et al.* Regulation of Macrophage Recognition through the Interplay of Nanoparticle Surface Functionality and Protein Corona. *ACS Nano* **10**, 4421–4430 (2016).

10. Tsoi, K. M. *et al.* Mechanism of Hard-Nanomaterial Clearance by The Liver. *Nat. Mater.* **15**, 1212–1221 (2016).

11. Lo Giudice, M. C., Herda, L. M., Polo, E. & Dawson, K. A. In Situ Characterization Of

534 Nanoparticle Biomolecular Interactions in Complex Biological Media by Flow
535 Cytometry. *Nat. Commun.* **7**, 1–10 (2016).
536 12. Bekdemir, A. & Stellacci, F. A Centrifugation-Based Physicochemical Characterization
537 Method for the Interaction Between Proteins and Nanoparticles. *Nat. Commun.* **7**, 1–8
538 (2016).
539 13. Shapero, K. *et al.* Time and Space Resolved Uptake Study of Silica Nanoparticles by
540 Human Cells. *Mol. Biosyst.* **7**, 371–378 (2011).
541 14. Saha, K. *et al.* Surface Functionality of Nanoparticles Determines Cellular Uptake
542 Mechanisms in Mammalian cells. *Small* **9**, 300–305 (2013).
543 15. Liu, M. *et al.* Real-Time Visualization of Clustering and Intracellular Transport of Gold
544 Nanoparticles by Correlative Imaging. *Nat. Commun.* **8**, 1–10 (2017).
545 16. Khlebtsov, N. & Dykman, L. Biodistribution and Toxicity of Engineered Gold
546 Nanoparticles: a Review of In Vitro and In Vivo Studies. *Chem. Soc. Rev.* **40**, 1647–
547 1671 (2011).
548 17. Almeida, J. P. M., Figueroa, E. R. & Drezek, R. A. Gold Nanoparticle Mediated Cancer
549 Immunotherapy. *Nanomedicine Nanotechnology, Biol. Med.* **10**, 503–514 (2014).
550 18. Loos, C. *et al.* Functionalized Polystyrene Nanoparticles as a Platform for Studying Bio-
551 Nano Interactions. *Beilstein J. Nanotechnol.* **5**, 2403–2412 (2014).
552 19. Talamini, L. *et al.* Influence of Size and Shape on the Anatomical Distribution of
553 Endotoxin-Free Gold Nanoparticles. *ACS Nano* **11**, 5519–5529 (2017).
554 20. Soenen, S. J. H. *et al.* Colloidal Gold Nanoparticles Induce Changes in Cellular and
555 Subcellular Morphology. *ACS Nano* **11**, 7807–7820 (2017).
556 21. Sandin, P. *et al.* The Biomolecular Corona is Retained During Nanoparticle Uptake and
557 Protects the Cells From the Damage Induced by Cationic Nanoparticles Until Degraded
558 in the Lysosomes. *Nanomedicine Nanotechnology, Biol. Med.* **9**, 1159–1168 (2013).

559 22. De Matteis, V. *et al.* Negligible Particle-Specific Toxicity Mechanism of Silver
560 Nanoparticles: the Role of Ag+ Ion Release in the Cytosol. *Nanomedicine*
561 *Nanotechnology, Biol. Med.* **11**, 731–739 (2015).
562 23. Arami, H., Khandhar, A., Liggitt, D. & Krishnan, K. M. In Vivo Delivery,
563 Pharmacokinetics, Biodistribution and Toxicity of Iron Oxide Nanoparticles. *Chem.*
564 *Soc. Rev.* **44**, 8576–8607 (2015).
565 24. Gao, C. *et al.* Y 2 O 3 Nanoparticles Caused Bone Tissue Damage by Breaking the
566 Intracellular Phosphate Balance in Bone Marrow Stromal Cells. *ACS Nano* **13**, 313–323
567 (2019).
568 25. Hu, W. *et al.* Protein Corona-Mediated Mitigation of Cytotoxicity of Graphene Oxide.
569 *ACS Nano* **5**, 3693–3700 (2011).
570 26. Walkey, C. D. *et al.* Protein Corona Fingerprinting Predicts the Cellular Interaction of
571 Gold And Silver Nanoparticles. *ACS Nano* **8**, 2439–2455 (2014).
572 27. Sabella, S. *et al.* A General Mechanism for Intracellular Toxicity of Metal-Containing
573 Nanoparticles. *Nanoscale* **6**, 7052–7061 (2014).
574 28. Jiang, Y. *et al.* The Interplay of Size and Surface Functionality on the Cellular Uptake
575 of Sub-10 nm Gold Nanoparticles. *ACS Nano* **9**, 9986–9993 (2015).
576 29. Corvaglia, S., Guarnieri, D. & Pompa, P. P. Boosting the Therapeutic Efficiency of
577 Nanovectors: Exocytosis Engineering. *Nanoscale* **9**, 3757–3765 (2017).
578 30. Kim, J. A., Aberg, C., Salvati, A. & Dawson, K. A. Role of Cell Cycle on the Cellular
579 Uptake and Dilution Of Nanoparticles In A Cell Population. *Nat. Nanotechnol.* **7**, 62–
580 68 (2012).
581 31. Rees, P. *et al.* Statistical Analysis of Nanoparticle Dosing in a Dynamic Cellular System.
582 *Nat. Nanotechnol.* **6**, 170–174 (2011).
583 32. Lee, J., Lilly, D., Doty, C., Podsiadlo, P. & Kotov, N. In Vitro Toxicity Testing of

584 Nanoparticles in 3D Cell Culture. *Small* **5**, 1213–1221 (2009).
585 33. Huang, K. *et al.* Size-Dependent Localization and Penetration of Ultrasmall Gold
586 Nanoparticles in Cancer Cells, Multicellular Spheroids, and Tumors In Vivo. *ACS Nano*
587 **6**, 4483–4493 (2012).
588 34. Huo, S. *et al.* Superior Penetration and Retention Behavior of 50 nm Gold Nanoparticles
589 in Tumors. *Cancer Res.* **73**, 319–330 (2013).
590 35. Mazuel, F. *et al.* Massive Intracellular Biodegradation of Iron Oxide Nanoparticles
591 Evidenced Magnetically at Single-Endosome and Tissue Levels. *ACS Nano* **10**, 7627–
592 7638 (2016).
593 36. Eisenstein, M. Organoids: The Body Builders. *Nat. Methods* **15**, 19–22 (2018).
594 37. Montenegro, J.-M. *et al.* In Vivo Integrity of Polymer-Coated Gold Nanoparticles. *Nat.*
595 *Nanotechnol.* **10**, 619–623 (2015).
596 38. Martinez, J. O. *et al.* Short And Long Term, In Vitro and In Vivo Correlations of Cellular
597 and Tissue Responses to Mesoporous Silicon Nanovectors. *Small* **9**, 1722–1733 (2013).
598 39. Yeung, C.-Y. *et al.* In Vivo Toxicologic Study of Larger Silica Nanoparticles in Mice.
599 *Int. J. Nanomedicine* **12**, 3421–3432 (2017).
600 40. Lopez-Chaves, C. *et al.* Gold Nanoparticles: Distribution, Bioaccumulation and
601 Toxicity. In Vitro and In Vivo Studies. *Nanomedicine Nanotechnology, Biol. Med.* **14**,
602 1–12 (2018).
603 41. Wyma, A. *et al.* Non-Newtonian Rheology in Suspension Cell Cultures Significantly
604 Impacts Bioreactor Shear Stress Quantification. *Biotechnol. Bioeng.* **115**, 2101–2113
605 (2018).
606 42. Davies, A. Cell Suspension Medium and Cell Suspension Medium Additive for the
607 Three Dimensional Growth of Cells. *Int. Pat.* **144372 Al**, (2013).
608 43. Curcio, E. *et al.* Mass Transfer and Metabolic Reactions in Hepatocyte Spheroids

609 Cultured in Rotating Wall Gas-Permeable Membrane System. *Biomaterials* **28**, 5487–
610 5497 (2007).
611 44. Panieri, E. & Santoro, M. M. ROS Homeostasis and Metabolism: A Dangerous Liason
612 in Cancer Cells. *Cell Death Dis.* **7**, e2253 (2016).
613 45. Davison, C. A. *et al.* Antioxidant Enzymes Mediate Survival of Breast Cancer Cells
614 Deprived of Extracellular Matrix. *Cancer Res.* **73**, 3704–3715 (2013).
615 46. Gloushankova, N. A., Rubtsova, S. N. & Zhitnyak, I. Y. Cadherin-Mediated Cell-Cell
616 Interactions in Normal and Cancer Cells. *Tissue Barriers* **5**, 1–15 (2017).
617 47. Pampaloni, F., Reynaud, E. G. & Stelzer, E. H. K. The Third Dimension Bridges the
618 Gap Between Cell Culture and Live Tissue. *Nat. Rev. Mol. Cell Biol.* **8**, 839–845 (2007).
619 48. Thornell, I. M. *et al.* Gel-Forming Mucins Form Distinct Morphologic Structures in
620 Airways. *Proc. Natl. Acad. Sci.* **114**, 6842–6847 (2017).
621 49. Endl, E. *et al.* The Expression of Ki-67, MCM3, and P27 Defines Distinct Subsets of
622 Proliferating, Resting, and Differentiated Cells. *J. Pathol.* **195**, 457–462 (2001).
623 50. Reinhardt, N., Adumeau, L., Lambert, O., Ravaine, S. & Mornet, S. Quaternary
624 Ammonium Groups Exposed at the Surface of Silica Nanoparticles Suitable for DNA
625 Complexation in the Presence of Cationic Lipids. *J. Phys. Chem. B* **119**, 6401–6411
626 (2015).
627 51. Adumeau, L. *et al.* Impact of Surface Grafting Density of PEG Macromolecules on
628 Dually Fluorescent Silica Nanoparticles Used for the In Vivo Imaging of Subcutaneous
629 Tumors. *Biochim. Biophys. Acta - Gen. Subj.* **1861**, 1587–1596 (2017).
630 52. Mahon, E., Hristov, D. R. & Dawson, K. A. Stabilising Fluorescent Silica Nanoparticles
631 Against Dissolution Effects for Biological Studies. *Chem. Commun.* **48**, 7970–7972
632 (2012).
633 53. Friedrich, J., Seidel, C., Ebner, R. & Kunz-Schughart, L. A. Spheroid-Based Drug

634 Screen: Considerations and Practical Approach. *Nat. Protoc.* **4**, 309–324 (2009).

635

636

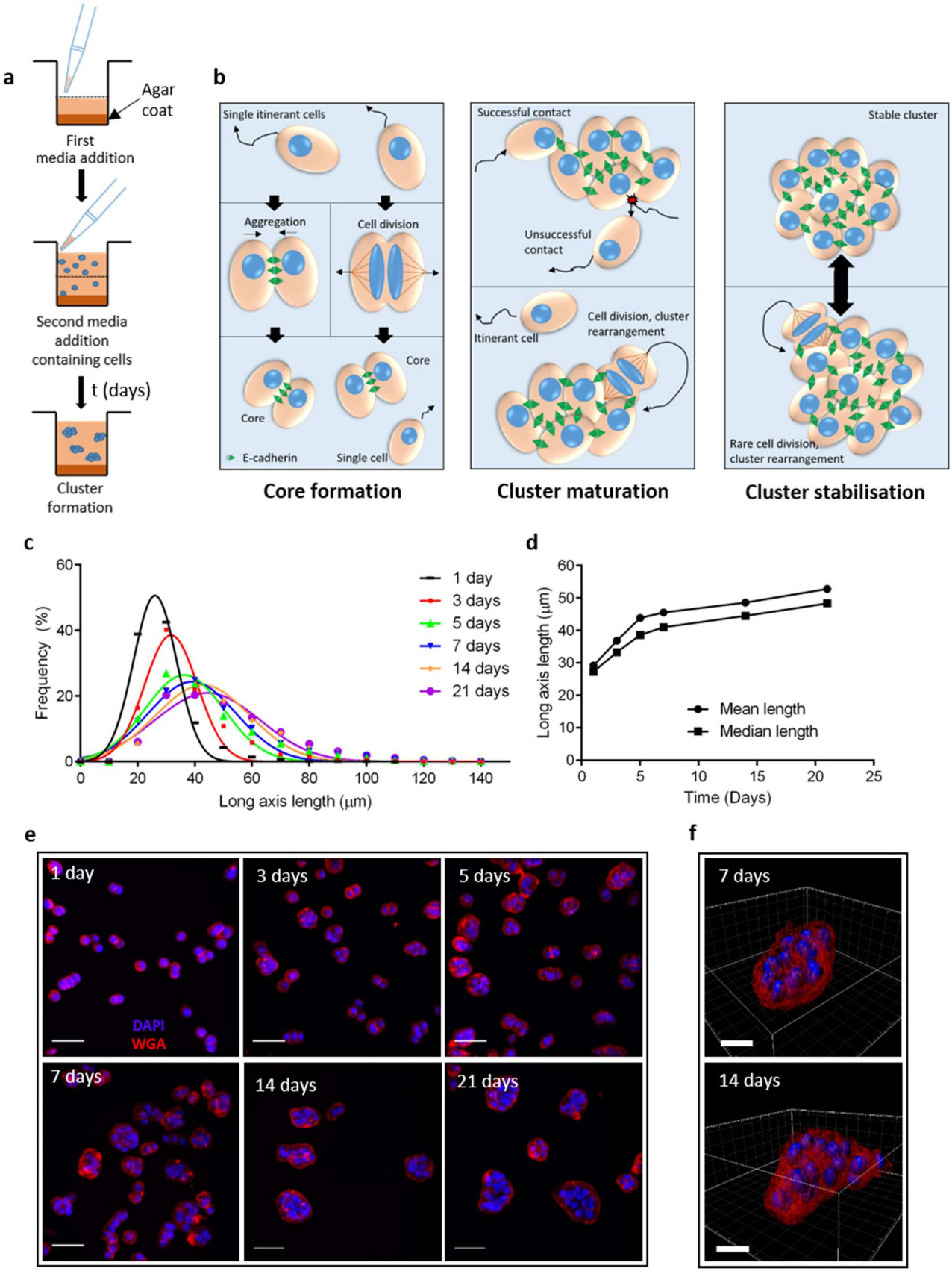

637

638 **Figure 1**: **Formation and evolution of the cell clusters**. **a,** Schematic illustration of the key

639 steps for cluster formation: an agar coating is first deposited to avoid cell attachment, and then

a layer of suspension media is added; cells are seeded on top of this layer to avoid excessive precipitation. **b**, Schematics of cluster formation and growth: when cells are suspended within the suspension media, several stages of cluster growth occur. In the first hours most cells are singlets and can move and divide more often. Some cells eventually come in contact and aggregate and so, in the second stage some clusters begin to form and become less mobile. In the third stage most clusters are fully formed, and further growth is limited. **c**, Gaussian fitting of the distribution of cell cluster diameters determined by high content analysis microscopy show that growth is more rapid in the first 5 days, and then slows thereafter. This is supported by **d,** extrapolation of the median and mean long axis length. **e,** Representative images of the clusters at different time-points showing the initial growth and then a more stationary phase. Nuclei are blue (DAPI) and plasma membrane is red (WGA547), scale bars = 50 μm. **f**, 3D reconstruction of clusters shows they are organised as an oblate shape and not spherical (scale bars = 20 μm).

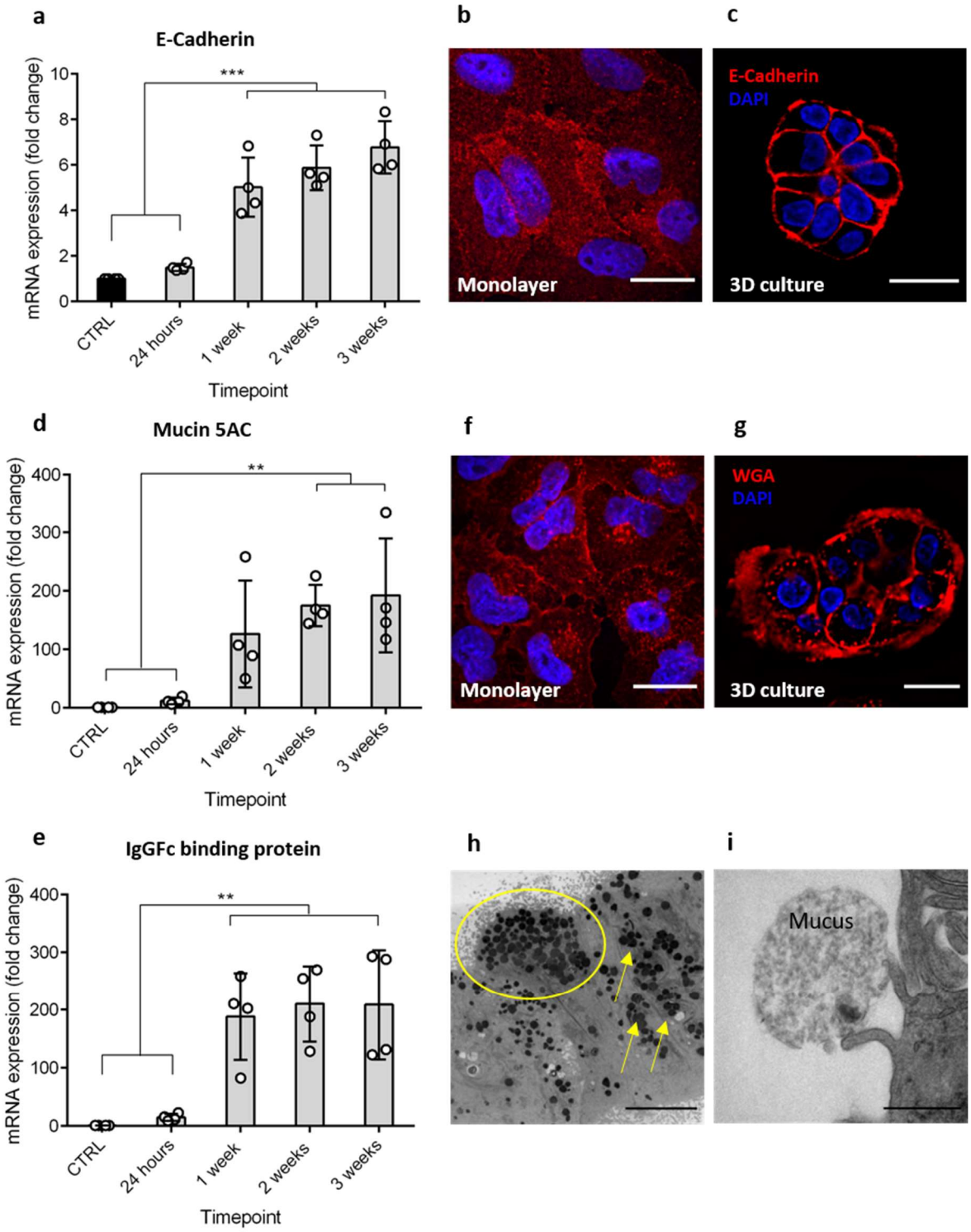

Figure 2: mRNA and protein expression analysis of the clusters suggests a differentiation of the cell phenotype towards a more *in vivo*-like representation. **a**, Increased E-cadherin gene expression in clusters, together with confocal imaging (**b** and **c**) reveals a stronger interaction between neighboring cells in suspension, compared to those grown in monolayer. **d,** A significant upregulation of mucin 5AC and IgG Fc binding protein (**e**) expression suggests

an increase of mucus secretion from cells in the clusters (N = 4 mean ± SD; * $p < 0.05$; ** $p < 0.01$; *** $p < 0.001$, calculated using one way ANOVA). This is supported by confocal image analysis of WGA stained monolayer cells (**f**) compared to 1 week old clusters (**g**) that show layers of mucus on the latter (scale bars = 20 μm). **h,** Representative TEM micrograph of a cell cluster after 3 weeks of culture shows very dense secretory granules in all the visible cells (circle and arrows; scale bar = 5 μm); **i**, mucus granules can be seen on the exterior of the cells (scale bar = 0.5 μm).

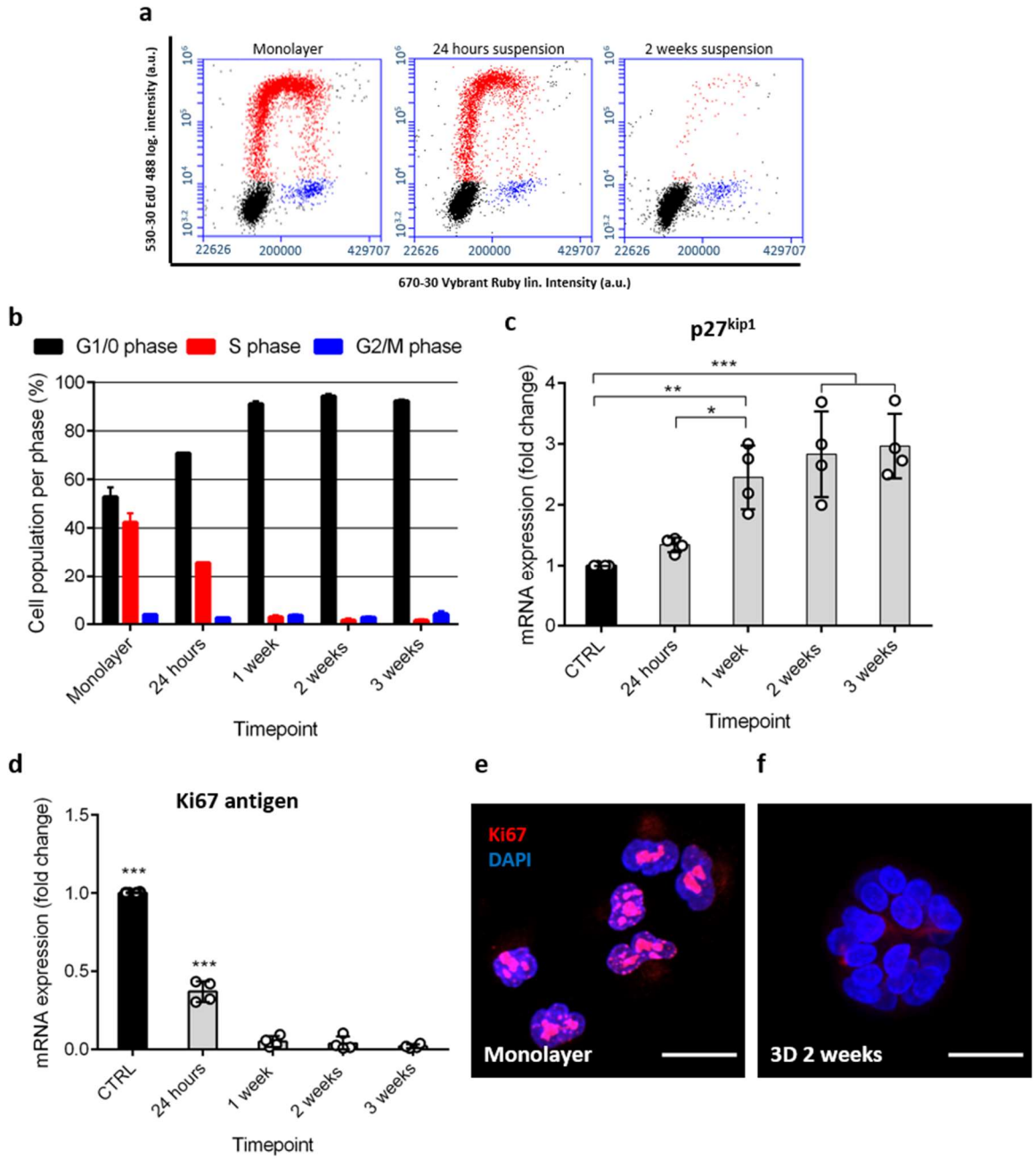

Figure 3: **Cells cultured as clusters exit the cell cycle and are maintained in a quiescent state**. **a**, EdU vs dsDNA content scatter plots obtained by flow cytometry analysis show changes in cell cycle phase distribution of monolayer and suspension cells after 24 hours and 2 weeks. **b**, The majority of cells are in the G0/1 phase after 1 week of suspension culture (N = 2, mean ± SD). **c**, Upregulation of $p27^{Kip1}$ (a cell cycle inhibitor) together with the downregulation of Ki67 (a proliferative cell marker) (**d**) suggests that the cells in clusters have exited the cell cycle (mean ± SD, N = 4; * $p < 0.05$; ** $p < 0.01$; *** $p < 0.001$, calculated using one way ANOVA); **e**, Immunocytochemical localisation of Ki67 shows that while the

680 protein is present in the nucleus of all cells in monolayer, in clusters (**f**) it is mostly absent
681 (scale bars = 20 μm).
682

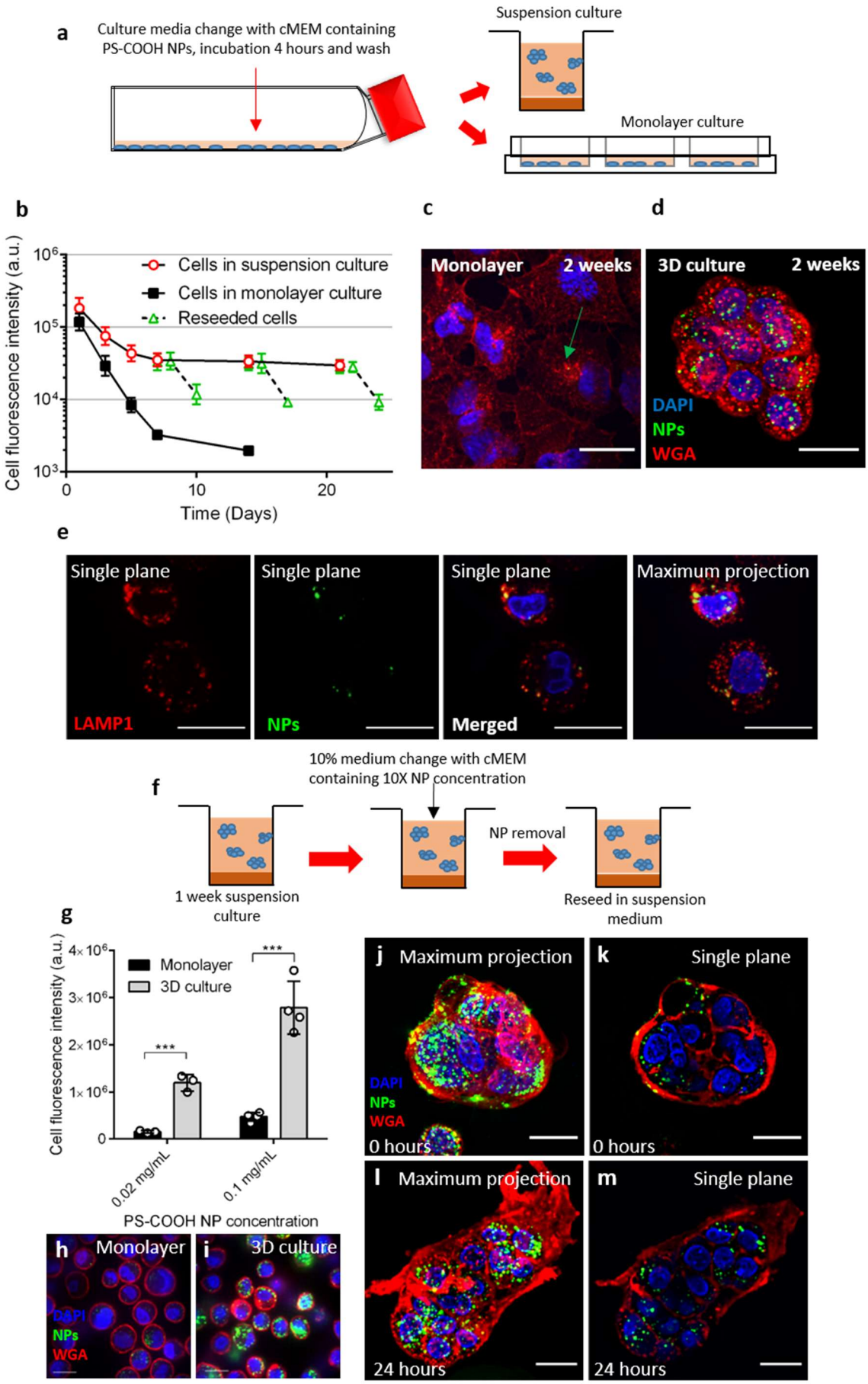
a
Culture media change with cMEM containing PS-COOH NPs, incubation 4 hours and wash
Suspension culture
Monolayer culture
b
Cell fluorescence intensity (a.u.)
Cells in suspension culture
Cells in monolayer culture
Reseeded cells
Time (Days)
c
Monolayer
2 weeks
d
3D culture
2 weeks
DAPI
NPs
WGA
e
Single plane
LAMP1
Single plane
NPs
Single plane
Merged
Maximum projection
f
10% medium change with cMEM containing 10X NP concentration
NP removal
1 week suspension culture
Reseed in suspension medium
g
Cell fluorescence intensity (a.u.)
Monolayer
3D culture
***
***
0.02 mg/mL
0.1 mg/mL
PS-COOH NP concentration
h
Monolayer
i
3D culture
DAPI
NPs
WGA
j
Maximum projection
k
Single plane
DAPI
NPs
WGA
0 hours
0 hours
l
Maximum projection
m
Single plane
24 hours
24 hours

Figure 4: **Evaluation of polystyrene nanoparticle accumulation in clusters**. **a**, Schematic illustration of nanoparticle treatment of cells in monolayer prior to cluster formation. **b**, The intracellular PS-COOH NP fluorecscence intensity for monolayer cells decreased continually, while for the clusters, after an initial decrease of signal in first week, there was no significant reduction thereafter (N = 3, mean ± SD). **c-d**, Confocal imaging of monolayer and cell clusters stained with WGA and DAPI 2 weeks from PS-COOH NP exposure shows that while few particles are detected in the monolayer cells, many are still present within the cells in clusters. **e**, LAMP1 immunostaining confirms nanoparticle localisation in lysosomes after 2 weeks of exposure in clusters. **f**, Schematic illustration of nanoparticle treatment of cells directly in clusters. **g**, There is a significantly higher uptake in clusters compared to monolayer (N = 3 for 0.02 mg/mL, N = 4 for 0.1 mg/mL; mean ± SD; *** $p < 0.001$, calculated using t-test). **h**, Confocal imaging of disassembled clusters confirms a higher nanoparticle content in cells in clusters compared to those in monolayer (**i**). **j,l**, maximum projection and (**k,m**) single Z-stack imaging of clusters treated with nanoparticles at 0h chase time (**j-k**) and 24 hours chase time (**l-m**) after treatment. Right after treatment many particles are still present on the surface of the clusters, while at 24 hours all particles seem to be internalised (all scale bars in this figure = 20 μm).

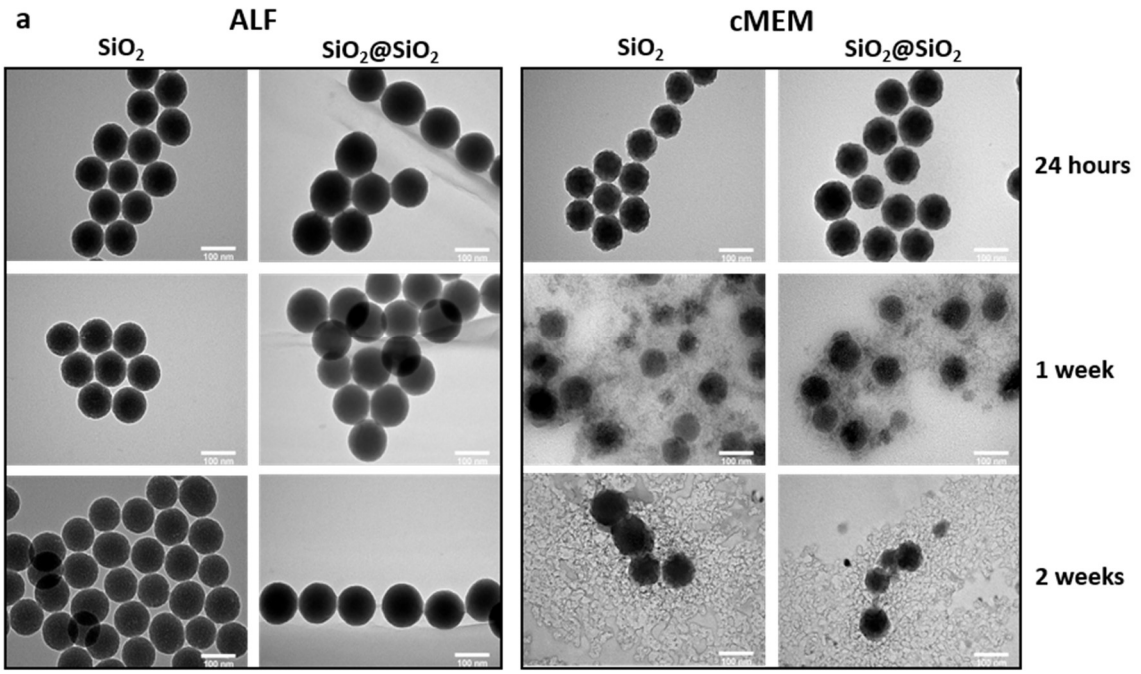
a
ALF
cMEM
SiO2
SiO2@SiO2
SiO2
SiO2@SiO2
24 hours
1 week
2 weeks

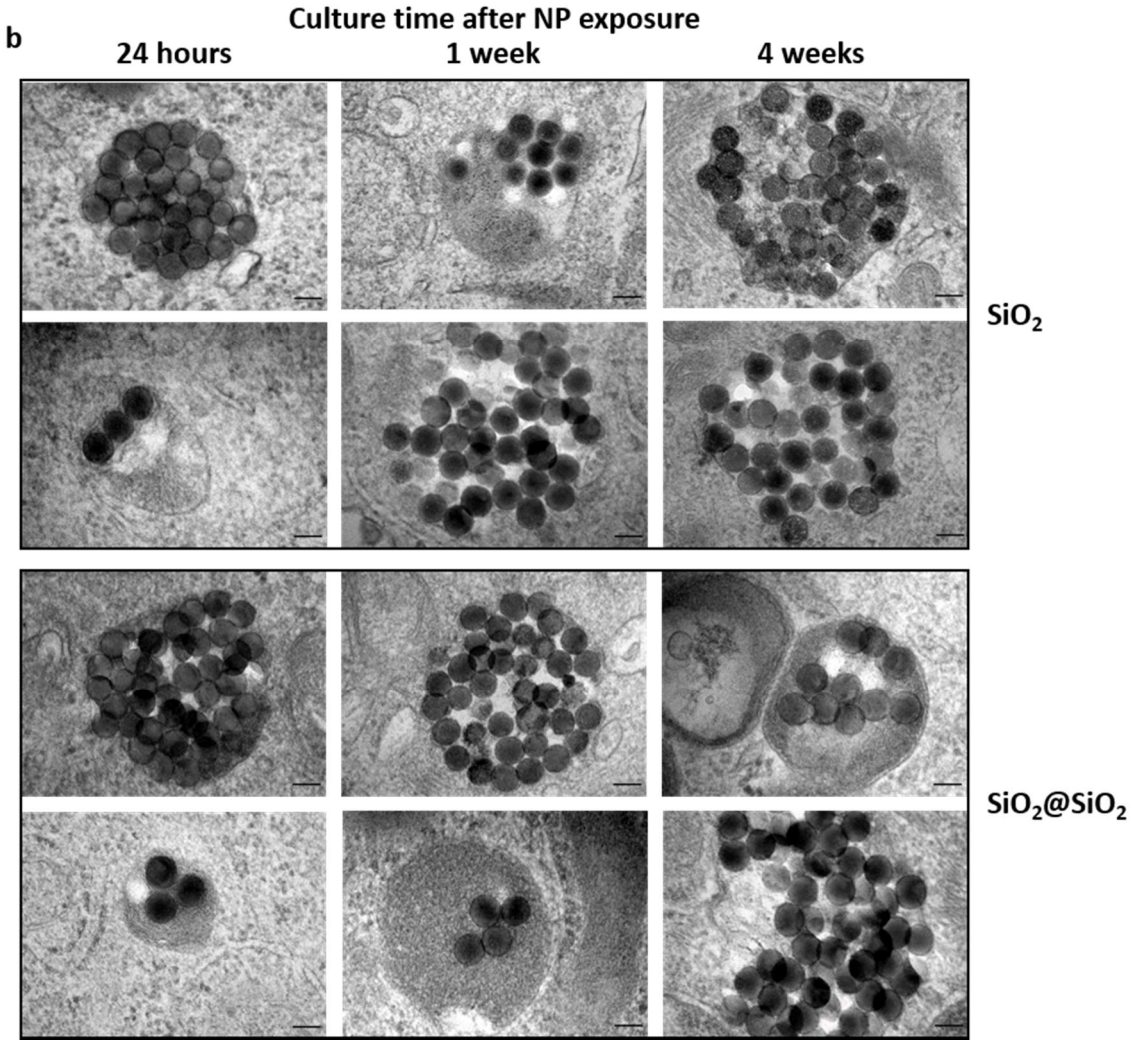
b
Culture time after NP exposure
24 hours
1 week
4 weeks
SiO2
SiO2@SiO2

702
703

Figure 5: **TEM micrographs of SiO_2 and SiO_2@SiO_2 NPs degradation in biological media and A549 cell clusters**. **a**, In cMEM both SiO_2 and SiO_2@SiO_2 nanoparticles show extensive degradation over a period of 2 weeks, while in artificial lysosomal fluid (ALF) no real effect is observed. **b**, In A549 cell clusters, while SiO_2@SiO_2 nanoparticles show only slight etching on their surfaces after 4 weeks, for non-coated SiO_2 nanoparticles a greater degradative effect due to lysosomal action can be observed over the culture duration (scale bars = 100 nm).